3D mapping of host-parasite-microbiome interactions reveals metabolic determinants of tissue tropism and disease tolerance in Chagas disease

Ekram Hossain[1,2], Sharmily Khanam[2,3], Chaoyi Wu[1,2], Sharon Lostracco-Johnson[4], Diane Thomas[4], Mitchelle Katemauswa[1], Camil Gosmanov[1], Danyang Li[5], Christine Woelfel-Monsivais[2,3], Krithivasan Sankaranarayanan [2,3]*, Laura-Isobel McCall [1,2,3]*

Affiliations:
[1]Department of Chemistry and Biochemistry, University of Oklahoma, Norman, Oklahoma, United States of America
[2]Laboratories of Molecular Anthropology and Microbiome Research, University of Oklahoma, Norman, Oklahoma, United States of America
[3]Department of Microbiology and Plant Biology, University of Oklahoma, Norman, Oklahoma, United States of America
[4]Skaggs School of Pharmacy and Pharmaceutical Sciences, University of California San Diego, La Jolla, California, United States of America
[5]College of Chemistry, Beijing Normal University, Beijing, China

E-mails:
ehossain@ou.edu
khanams@ou.edu
chaoyiwu0810@ou.edu
sharizzy@gmail.com
d4thomas@ucsd.edu
mitchelle.katemauswa@ou.edu
camil@ou.edu
201611150915@mail.bnu.edu.cn
christinewm@ou.edu
ksankar@ou.edu
lmccall@ou.edu

* Correspondence for 16S analyses to Krithivasan Sankaranarayanan, ksankar@ou.edu
Correspondence for LC-MS/MS, Chagas disease, and overall project design to Laura-Isobel McCall, lmccall@ou.edu

42   **Abstract:** Chagas disease (CD) is a parasitic infection caused by *Trypanosoma cruzi* protozoa.

43   Over 8 million people worldwide are *T. cruzi*-positive, 20-30% of which will develop

44   cardiomyopathy, megaoesophagus and/or megacolon. The mechanisms leading to

45   gastrointestinal (GI) symptom development are however poorly understood. To address this

46   issue, we systematically characterized the spatial impact of experimental *T. cruzi* infection on the

47   microbiome and metabolome across the GI tract. The largest microbiota perturbations were

48   observed in the proximal large intestine in both acute and chronic disease, with chronic-stage

49   effects also observed in the cecum. Strikingly, metabolomic impact of acute-to-chronic stage

50   transition differed depending on the organ, with persistent large-scale effects of infection

51   primarily in the oesophagus and large intestine, providing a potential mechanism for GI

52   pathology tropism in CD. Infection particularly affected acylcarnitine and lipid metabolism.

53   Building on these observations, treatment of infected mice with carnitine-supplemented drinking

54   water prevented acute-stage mortality with no changes in parasite burden. Overall, these results

55   identified a new mechanism of disease tolerance in CD, with potential for the development of

56   new therapeutic regimens. More broadly, these results highlight the potential of spatially-

57   resolved metabolomic approaches to provide insight into disease pathogenesis, with translational

58   applications for infectious disease drug development.

59

60   **Introduction:** Chagas disease (CD), also known as American trypanosomiasis, is a neglected

61   tropical disease endemic in Latin America [1]. However, due to migration CD now has a global

62   reach spanning North America, Europe and Asia [2]. Six to eight million people are infected with

63   *T. cruzi,* with approximately 12,000 deaths per year [3]. CD is caused by infection with the

64   protozoan parasite *Trypanosoma cruzi*. Infected individuals pass first through an acute disease

65   stage, usually asymptomatic, then to a chronic asymptomatic (indeterminate) stage that can last

66   for decades. Thirty to forty percent of infected individuals progress from indeterminate to

67   determinate (symptomatic) chronic CD [4], 20-30% with cardiovascular complications (heart

68   failure, arrhythmias, and thromboembolism) and 15-20% of infected individuals with

69   gastrointestinal (GI) symptoms (megaesophagus and megacolon) [5]. Digestive CD has been

70   neglected compared to cardiac CD and consequently is much more poorly understood. However,

71   recent studies using bioluminescent parasites in mouse models have shown that specific sites in

72   the GI tract are parasite reservoirs in chronic CD and may be major contributors to cardiac

73   symptom development, particularly after treatment failure [678]. Treatment of GI CD is also

74   challenging, with limited options once symptoms become apparent [1]. There is therefore a strong

75   need to improve our understanding of the interaction between *T. cruzi* and the GI tract, both to

76   clarify mechanisms of GI CD pathogenesis, and to define GI factors contributing to cardiac CD,

77   leading to new treatment strategies.

78   The GI tract is a complex environment where host, pathogen and microbiota interact to

79   affect disease pathogenesis [9]. We previously demonstrated that *T. cruzi* infection affects the fecal

80   microbiome and metabolome, but information on the specific GI sites driving this output had not

81   yet been determined [10]. In this study, we applied a novel integration of small molecule-focused

82   liquid chromatography-tandem mass spectrometry (LC-MS/MS) and 3D modeling ("chemical

83   cartography"), in conjunction with microbiome analysis, to systematically characterize the *T.*

84   *cruzi*-induced changes in the GI microenvironment in acute and chronic CD. We specifically

85   focused on small molecule characterization because they represent the output of cellular

86   processes as well as their regulators, and therefore have the closest relationship to phenotype [11].

87   Given that most drugs are still small molecule-based [12], we further hypothesized that identifying

88   infection-associated disturbances in the small molecule profile can most rapidly lead to new

89   treatments for CD.

90   Results identified organ-specific and organ sub-site-specific magnitudes of disruptions in

91   the chemical and microbial GI environment by *T. cruzi,* and highlighted differential mechanisms

92   of acute to chronic stage transitions depending on organ. These results provide a mechanism by

93   which consistent perturbations of tissue biochemical pathways lead to GI CD pathology in the

94   oesophagus and large intestine. Consistent infection-induced elevation of acylcarnitine family

95   members across organs further led us to investigate the role of acylcarnitines in disease

96   pathogenesis. Supplementing animal drinking water with carnitine prevented acute-stage

97   mortality in experimental CD in the absence of antiparasitic effect, revealing a novel mechanism

98   of disease tolerance in CD. Overall, these results identified novel mechanisms of CD

99   pathogenesis, with major translational applications to CD drug development. Furthermore, the

100   data collected here on uninfected animals, and our approach in general, can serve as a reference

101   to investigate determinants of tropism and novel treatment strategies for any other GI pathogen.

102

103

Results:

Regiospecific molecular impact of *T. cruzi* colonization in the GI tract

104

105

106   GI CD is still poorly understood. In our prior work, we identified specific small

107   molecules correlated with cardiac parasite tropism [13]. Here, we sought to identify the

108   locoregional chemical changes associated with parasite GI colonization. Mice were infected with

109   1,000 luciferase-expressing *T. cruzi* strain CL Brener parasites [6]. Twelve days (acute stage) and

110   89 days (chronic stage) post-infection, animals were euthanized, the GI tract sectioned (**Fig.**

111   **S1a**), and parasite burden in each section determined by *ex vivo* bioluminescence imaging (**Fig.**

112   **1abc**). At 12 days post infection, parasite burden was high throughout the GI tract, with the

113   highest parasite burden in the distal small intestine (position 9; $p<0.05$ Student's T-test, distal

114   small intestine to mid and distal stomach, small intestine position 6 and small intestine position

115   7), and the lowest parasite burden in the cecum (position 10, $p<0.05$ Student's T test cecum vs

116   oesophagus, distal small intestine and distal large intestine; **Fig. 1ab)**. In contrast, at 89 days

117   post-infection, the parasite burden was highest in the cecum ($p<0.05$ Student's T-test, cecum vs

118   oesophagus, proximal and distal small intestine), and lowest in the proximal small intestine

119   ($p<0.05$ Student's T-test, small intestine positions 5 and 6 vs oesophagus, proximal and distal

120   large intestine, **Fig. 1ac**). In general, as expected, parasite burden decreased from the acute stage

121   to the chronic stage (**Fig. S1b**). However, surprisingly, parasite burden increased in the cecum

122   during the acute to chronic transition, suggesting a possible role for the cecum as a parasite

123   reservoir protected from antiparasitic immune responses (**Fig. S1b**). These observations support

124   the concept that all GI sites can initially harbor *T. cruzi,* but then differentially respond to

125   parasite presence, leading to the ability of the parasite to persist and cause damage in some sites

126   but not others.

127   Given this differential parasite tropism in the chronic stage and the unique aspects of CD

128   pathology, we sought to investigate the molecular determinants of parasite persistence vs disease

129   resolution. To do so, we extracted small molecules (metabolites) from each collected GI section

130   (637 samples total) and analyzed these molecules by LC-MS/MS in positive and in negative

131   mode. As expected, the strongest determinant of overall chemical profile was the source organ,

132   and sample position within that organ, as observed by principal coordinate (PCoA) analysis (**Fig.**

133   **1d,** PERMANOVA based on source organ, $p<0.001$, $R^2=46.374\%$ for positive mode LC-MS/MS

134   analysis and $p<0.001$, $R^2=47.033\%$ for negative mode LC-MS/MS analysis; PERMANOVA

4

135   based on sampling position, p<0.001, R^2=13.494% for positive mode LC-MS/MS analysis and

136   p<0.001, R^2=16.477% for negative mode LC-MS/MS analysis (12 days post-infection);

137   PERMANOVA based on sampling position, p<0.001 R^2=12.067% positive mode and p<0.001

138   R^2=13.918% negative mode (all timepoints combined)). Overall impact of infection was much

139   more minor (**Fig. S2, S3,** PERMANOVA based on infection status, acute stage, p=0.019,

140   R^2=1.011% for positive mode LC-MS/MS analysis and p=0.07, R^2=0.692% for negative mode

141   LC-MS/MS analysis; PERMANOVA based on infection status, chronic stage, p=0.014,

142   R^2=0.982% for positive mode LC-MS/MS analysis and p=0.007, R^2=0.981% for negative mode

143   LC-MS/MS analysis). Comparison of chemical families differentially-modulated by infection

144   also identified few commonalities between sample sites (**Fig. S4, S5**). We therefore focused our

145   analysis on the impact of infection in each individual organ. Visualization of the chemical profile

146   in each organ in relationship to infection status using PCoA analysis revealed organ-specific

147   differences in the impact of *T. cruzi* infection. Acute-stage infection was associated with major

148   disturbances in the overall oesophagus chemical profile (PERMANOVA p=0.002, R^2=15.871%),

149   with lower-scale perturbations in the small intestine and cecum (PERMANOVA p<0.001,

150   R^2=6.95% and PERMANOVA p=0.02, R^2=10.411%, respectively) (**Fig. 1e, S6**). The strongest

151   acute-stage disruption within the small intestine chemical environment was observed in the distal

152   small intestine, where parasite burden is the highest (**Fig. 1e,** PERMANOVA p<0.001,

153   R^2=30.198%; p<0.001, R^2=26.063; p=0.006, R^2=12.564, for positions 7, 8, 9, respectively).

154   These changes resolved in the chronic stage for the cecum (PERMANOVA p=0.171,

155   R^2=6.955%), decreased in magnitude for the small intestine (PERMANOVA p<0.001,

156   R^2=4.824), became apparent in the stomach and large intestine (PERMANOVA p=0.021,

157   R^2=4.429% and PERMANOVA p=0.008, R^2=6.323%, respectively), and increased in magnitude

158   in the oesophagus (PERMANOVA p<0.001, R^2=38.061%). Importantly, the largest statistically

159   significant sites of metabolome disturbance in the chronic stage were the oesophagus and large

160   intestine, which are the sites of damage in symptomatic chronic-stage GI CD [14]. On a per-

161   sampling site basis, spatial heterogeneity in terms of overall effect size (R^2) was observed within

162   a given organ. The largest increase in R^2 during the transition from the acute to the chronic stage

163   were observed in the oesophagus, distal stomach and central large intestine (2.4, 2.0 and 1.9-fold

164   increases, respectively).

165   Next, we investigated the nature of the chemical shifts associated with these infection-

166   altered chemical profiles. Feature annotation rates were considerably higher in positive mode

167   than in negative mode (35.4% vs 10.2%), so we focused this analysis on our positive mode LC-

168   MS/MS data. We used machine learning (random forest) approaches to identify specific

169   molecular features driving the differences between infected and uninfected tissues. Given our

170   observations on the impact of sampling position on metabolite features (PCoA, **Fig. 1d, Fig. S2,**

171   **Fig. S3, Fig. S5**), these comparisons were independently performed for each organ. In the acute

172   stage, we observed elevation in specific acylcarnitines and specific phosphatidylcholine (PC)

173   family members in the different organs (**Fig. 2a-f,Table S1, Fig. S7**). We also observed

174   elevation in kynurenine in the stomach and large intestine in the acute stage. These differences

175   persisted in the chronic stage for the proximal and central large intestine only (**Fig. 2g-h,Table**

176   **S1, Fig. S7**). Strikingly, the levels of tryptophan, the precursor of kynurenine, were

177   correspondingly decreased in the acute stage at the same large intestine sites where kynurenine

178   was elevated, whereas it was increased by infection in the chronic stage in the oesophagus (**Fig.**

179   **2i-j**). Kynurenine is induced by inflammation; kynurenine metabolites have direct antiparasitic

180   effects and contribute to the control of acute *T. cruzi* infection [15]. However, they can also induce

181   regulatory T cells [16], and as such, our observation of kynurenine persistence in the large intestine

182   may contribute to parasite persistence in this organ. In accordance with our prior observations in

183   the context of the fecal metabolome [10], specific large intestine and small intestine bile acid

184   derivatives were increased in infected mice (**Fig. 2k-m, Table S1, Fig. S7**). At 89 days post-

185   infection, molecular features identified as elevated by infection include specific acylcarnitines

186   (*e.g.* C20:4 acylcarnitine in the oesophagus), specific PCs (*e.g.* PC(22:5), PC(20:4), PC(22:6) in

187   the oesophagus; PC(22:4) in the large intestine), specific amino acids and derivatives (*e.g.*

188   kynurenine in the large intestine, tryptophan in the oesophagus) (**Fig. 2a-j, Table S1, Fig. S7**).

189   Importantly, the pattern of persistence of these metabolic changes reflected known sites of CD:

190   for example, most of the top 10 metabolic perturbations observed in the acute stage in the

191   oesophagus were still perturbed by infection in the chronic stage, whereas none of the small

192   intestine acute-stage perturbations persisted in the chronic stage (**Fig. 2, Table S1**). Overall,

193   these results identified tissue metabolic changes linked to CD tropism and pathogenesis, at the

194   scale of overall chemical disturbances, as well as several metabolic pathways correlated with

195   infection status.

196

Impact of *T. cruzi* colonization on the GI tract microbiome

198   Several of the molecules identified in our dataset are of microbial origin or microbially-

199   modified, such as indole-L-lactate, indoxyl sulfate and secondary bile acids (**Fig. S8, Table S2**).

200   Dataset match analysis through the GNPS platform [17] identified 1689 unique matches in our

201   positive mode dataset to pure bacterial culture datasets not shared with pure mammalian culture

202   datasets, known plastics-derived contaminants or blank files, suggesting a potential bacterial

203   origin. Studies comparing germ-free and colonized mice have also shown that the microbiota

204   influences a variety of the metabolites detected in our study, including tryptophan, tyrosine and

205   maltotriose [18,19]. Tryptophan and tyrosine in particular were affected by infection (tryptophan:

206   decreased in the large intestine overall, Mann-Whitney p=6.793e-06 (acute stage) and

207   p=0.004313 (chronic stage); tyrosine: decreased in the large intestine overall, Mann-Whitney

208   p=0.01518 (acute stage), non-significant (chronic stage)). We have previously demonstrated that

209   experimental *T. cruzi* infection alters the fecal microbiome and metabolome [10], a finding that was

210   recently confirmed in *T. cruzi*-infected children in Bolivia [20]. We therefore sought to evaluate the

211   spatial impact of *T. cruzi* infection on the microbiota at each collection site in acute-stage disease

212   (except for the oesophagus where insufficient material was available to perform both

213   metabolomic and 16S analyses), and focusing on the cecum and large intestine in chronic

214   disease, given their role as major sites of CD pathogenesis and the unique metabolomic pattern

215   observed at these sites (**Fig. 1e**).

216   Differences in the overall microbiota composition (beta-diversity, all sites combined for a

217   given organ) were observed in the stomach and large intestine in the acute stage (PERMANOVA

218   p=0.05, R^2=3.22% and PERMANOVA p=0.04, R^2=3.837%, respectively), with non-significant

219   changes in the small intestine and cecum (PERMANOVA p=0.069, R^2=1.791% and

220   PERMANOVA p=0.058, R^2=10.657%, respectively). These differences increased in magnitude

221   for the cecum and large intestine during the transition from acute to chronic stage

222   (PERMANOVA p=0.02, R^2=11.556% and PERMANOVA p=0.002, R^2=5.83%, respectively)

223   (**Fig. 3a-f**). Spatial heterogeneity was also observed within an organ (**Fig. 3g**), with the highest

224   disturbances in the microbiota found in the proximal large intestine (sampling position 11,

225   PERMANOVA p=0.022, R^2=12.36% and PERMANOVA p=0.009, R^2=10.715% for acute and

226   chronic stage, respectively). Persistent disturbances in the large intestine microbiota reflect our

227   findings for the large intestine metabolome, while the discrepancies between cecal microbiota

228   and metabolome findings may reflect persistent luminal rather than tissue alterations. Overall,

229   the persistence of microbiota alterations in these sites correlates well with our observation of

230   continued alterations of the fecal microbiota and metabolome through acute and chronic

231   experimental CD [10]. In accordance with prior reports [20,10], no significant differences in alpha-

232   diversity were observed (**Fig. S9**) between infected and uninfected tissue in both acute and

233   chronic stages. Notably, the effect size observed for microbiota composition analysis was lower

234   than for our tissue metabolomics analysis (**Fig. 1**), although in both cases the proximal large

235   intestine was one of the major sites of infection-associated perturbation. This may reflect

236   segregation of the microbiome from the site of infection, so that only indirect effects can be

237   observed. Furthermore, cage and batch effects were found to have a larger impact on microbiome

238   composition (**Fig. S10**), while metabolome analysis was more robust to such effects, as we

239   previously reported [10].

240

241   **Role of acylcarnitines in CD tolerance**

242   Translating 'omics findings into novel therapeutic approaches is one of the major

243   challenges of this post-genome era. Because we observed larger metabolome than microbiome

244   infection-associated perturbations, and based on our current observations of infection-induced

245   elevation in specific acylcarnitine family members, and our prior findings of differential cardiac

246   acylcarnitine distribution and mass range in mild vs severe acute *T. cruzi* infection [13], we focused

247   here on acylcarnitines and the potential of acylcarnitine modulation for CD treatment. The

248   acylcarnitine sub-network (**Fig. 4a**) was manually annotated (**Table S3, Fig. S11a**), and impacts

249   of infection on short-chain (C3-C4), mid-chain (C5-C11) and long-chain (C12 and greater)

250   acylcarnitines assessed. While total and short-chain GI short-chain acylcarnitine levels were

251   comparable between infected and uninfected animals 12 days post-infection (**Fig. S11bc**), we

252   observed significant elevation in total and short-chain acylcarnitine levels at each small intestine

253   site, in infected animals (total acylcarnitines: FDR-corrected Mann-Whitney p=0.00543,

254   p=0.000422, p=7.04e-05, p=7.04e-05, p=0.000422 for positions 5, 6, 7, 8, 9; short-chain

255   acylcarnitines: FDR-corrected Mann-Whitney p=0.000668, p=0.000563, p=0.000141,

256   p=0.000563, p=0.00189 for positions 5, 6, 7, 8, 9; **Fig. S11de**). For long-chain acylcarnitines,

257   infection-induced acylcarnitine elevation was restricted to the distal portions of the small

258   intestine (FDR-corrected Mann-Whitney p=0.000141, p=0.000563, p=0.000563 for positions 7,

259   8, 9; **Fig. 4bc**). This difference between total and spatially-resolved short-chain acylcarnitine

260   levels highlight the strength of our chemical cartography approach. Mid-chain (C5 to C11)

261   acylcarnitine levels were not significantly different 12 days post-infection between infected and

262   uninfected animals at any GI site (**Fig. S11f**). Acylcarnitine small intestine elevation was no

263   longer observed in the chronic stage, except for short-chain acylcarnitines in the duodenum

264   (sampling position 5, FDR-corrected Mann-Whitney p=0.0253), although select other GI sites

265   showed infection-induced increases in acylcarnitines (**Fig. S11ghi**; distal large intestine, total

266   acylcarnitines and short-chain acylcarnitines, FDR-corrected Mann-Whitney p=0.0196 and

267   p=0.0387, respectively; oesophagus, short-chain acylcarnitines, FDR-corrected Mann-Whitney

268   p=0.00422). Acetyl-carnitine was also elevated in select sites 12 days post-infection (FDR-

269   corrected Mann-Whitney p=0.0.0220, p=0.003413, p=0.000141, p=0.000141, p=0.0008913,

270   p=0.0220 for sites number 4-9 (stomach and small intestine, 12 days post-infection)), but was

271   comparable between infected and uninfected tissues at all sites 89 days post-infection (**Fig.

272   S11jk**). In contrast, unmodified carnitine levels were comparable throughout the intestine 12

273   days post-infection, and only significantly elevated in infected oesophagus and uninfected central

274   large intestine 89 days post-infection (FDR-corrected Mann-Whitney p=0.000141 and p=0.

275   0187, respectively) (**Fig. S11l**).

276   To determine whether we could translate these findings towards novel CD therapeutics

277   and whether these acylcarnitine alterations play a causal role in disease progression, we assessed

278   whether carnitine supplementation could alter acute CD outcome. Mice were infected with either

279   an intermediate dose (5,000 trypomastigotes) or a high dose (50,000 trypomastigotes) of

280   luciferase-expressing CL Brener parasites [6]. At 7 days post-infection, animals were distributed

281   into two groups of comparable parasite burden and one group switched from normal drinking

282   water to drinking water supplemented with L-carnitine (equivalent to 100 mg/kg/day based on

283   water consumption). Carnitine treatment completely abrogated acute CD-induced mortality up to

284   7 weeks post-infection (**Fig. 4d,** p=0.0027 Mantel-Cox test, 50,000 trypomastigote infection;

285   **Fig. S12a**), but without any effect on parasite burden or parasite distribution (**Fig. 4ef, S12b**).

286   This lack of antiparasitic activity is consistent with prior *in vitro* activity data showing no impact

287   of carnitine on parasite burden [21]. Overall, these results indicate that acylcarnitine modulation by

288   carnitine supplementation can induce disease tolerance in CD. These results have important

9

289   implications for our understanding of the factors that contribute to the progression from

290   asymptomatic to symptomatic CD, and represent a novel avenue for CD drug development, in

291   conjunction with antiparasitics to kill *T. cruzi*.

292

Discussion:

294   Disease severity is tied to the balance between resistance and tolerance mechanisms [22].

Resistance reduces pathogen load, but can cause collateral damage to the host, as indeed has

been observed with immune clearance of *T. cruzi*-infected cells [23]. In contrast, tolerance reduces

disease or immune-mediated collateral damage without affecting the pathogen load [22]. While

parasite persistence is required for progression to chronic CD [24], only a minority of infected

patients progress to symptomatic disease [4], and parasite load does not fully predict disease

severity (*e.g.* [25]), indicating that disease tolerance mechanisms also regulate CD progression,

although these are not well understood. Our novel finding that carnitine modulation determines

infection outcome (**Fig. 4**) paves the way for future studies of the role of acylcarnitines in the

progression from asymptomatic to symptomatic disease in humans, as well as the development

of novel interventional strategies for CD, most likely in combination with antiparasitic agents.

Our observations also represent the first time that carnitine metabolism has been directly linked

to disease tolerance mechanisms, rather than serving as a readout for altered fatty acid

metabolism. Importantly, acylcarnitines, as with many other infection-modulated metabolites in

our dataset, showed strong spatial effects that would have been masked by bulk tissue analysis,

demonstrating the strength of this spatially-resolved approach (**Fig. 2, Fig. 4b, Fig. S11**).

Strikingly, sites of largest statistically significant overall metabolic disturbance in the chronic

stage were the oesophagus and large intestine (**Fig. 1**), providing a mechanism whereby

persistent metabolic alterations at these sites drive the striking selective tropism of CD for the

large intestine and oesophagus. In contrast, chronic parasite persistence in the cecum was

metabolically silent (**Fig. 1**), while cecal microbiome remained strongly and significantly

affected by infection (**Fig. 3**). It is tempting to speculate a microbiota-mediated mechanism of

reduced antiparasitic immune responses in the cecum, perhaps via cecal microbiota-derived

short-chain fatty acid [26], or induction of parasite dormancy at this site [27], leading to the observed

parasite recrudescence in the cecum following incomplete posaconazole or nifurtimox treatment

[828], and this awaits further experimentation. Lastly, the spatially-resolved metabolomic and

10

320 microbiome methods that we illustrate here with *T. cruzi* can readily be applied to study other

321 pathogens with specific tissue tropism, and we anticipate this approach to have broad

322 applicability. Likewise, initial pathogen tropism is affected by tissue characteristics. Our

323 comprehensive spatial characterization of the microbiome and metabolome of uninfected animals

324 therefore represents a resource that can serve as a hypothesis-generating starting point for studies

325 of pathogen tropism.

326

327 **Methods:**

328 *In vivo* **experimentation**: All vertebrate animal studies were performed in accordance with the

329 USDA Animal Welfare Act and the Guide for the Care and Use of Laboratory Animals of the

330 National Institutes of Health. The protocol was approved by the University of California San

331 Diego Institutional Animal Care and Use Committee (protocol S14187).

332   For chemical cartography and 16S analysis: 5-week-old male C3H/HeJ mice (The

333 Jackson Laboratory) were infected by intraperitoneal injection of 1,000 red-shifted luciferase-

334 expressing *T. cruzi* strain CL Brener [6] culture-derived trypomastigotes in 100 μL DMEM media

335 (infected group) or mock-infected by injection of 100 μL DMEM media only (uninfected group).

336 Prior to animal infection, *T. cruzi* parasites were maintained in coculture with C2C12 mouse

337 myoblasts, in DMEM (Invitrogen) supplemented by 5% iron-supplemented calf serum

338 (HyClone) and 1% penicillin-streptomycin (Invitrogen). Twelve or 89 days post-infection,

339 animals were injected with 150 mg/kg D-luciferin potassium salt (Gold Biotechnology) and

340 euthanized by isoflurane overdose followed by cervical dislocation. Mice were then immediately

341 perfused with 10 mL of 0.3 mg/mL ice-cold D-luciferin in PBS [6]. GI organs were collected,

342 sectioned as displayed on **Fig. S1a** and each section placed in an individual 96-well-plate well

343 containing 0.3 mg/mL ice-cold D-luciferin in PBS [6]. The plate was imaged in an *In vivo* Imaging

344 System (IVIS) Lumina LT Series III (Perkin Elmer) and tissues were then immediately snap-

345 frozen in liquid nitrogen, followed by storage at -80 ºC. Tissue section luminescence was

346 determined using Living Image 4.5 software, normalized to collected tissue weight, and plotted

347 using GraphPad Prism version 8. Two biological replicate experiments were performed, each

348 including n=5 mice for each timepoint and infection condition (total n=10 per timepoint and

349 infection condition). The same samples were used as source material for 16S and LC-MS

350 analysis (see below), with each tissue site from each individual animal representing a single data

351 point in each analysis.

352   For carnitine supplementation experiments: mice were infected with either an

353 intermediate dose (5,000 culture-derived trypomastigotes) or a high dose (50,000 culture-derived

354 trypomastigotes) of red-shifted luciferase-expressing CL Brener parasites [6]. Seven days post-

355 infection, mice were injected with 150 mg/kg D-luciferin potassium salt (Gold Biotechnology)

356 and imaged (IVIS Lumina LT Series III). Animals were allocated to treatment groups to have

357 comparable total body luminescence signal between groups. Mice then received L-carnitine

358 (VWR) in drinking water *ad libitum,* normalized to mouse water consumptions so that animals

359 received ca. 100 mg/kg/day, or regular drinking water (n=5 per group). Bioluminescent imaging

360 was performed weekly. Animals reaching humane endpoints of weight loss >20% were

361 euthanized. Bioluminescence data was analyzed with Living Image 4.5 software and plotted

362 using GraphPad Prism version 8.

363

364 **Sample preparation for LC-MS/MS:** Samples from both biological replicate experiments were

365 analyzed jointly. Metabolites were extracted from the collected tissue samples using a two-step

366 process as implemented in our prior work [13], normalizing to tissue weight. Tissue samples were

367 homogenized in LC-MS grade water (50 mg tissue in 125 µL water) using a 5 mm steel ball in

368 Qiagen TissueLyzer at 25 Hz for 3 min. 10 µL was set aside for DNA extraction and microbiome

369 profile analysis, except for oesophagus where the tissue amount was too small. LC-MS grade

370 methanol spiked with 4 µM sulfachloropyridazine was added to the homogenized sample, to a

371 final concentration of 50% methanol, and the sample was homogenized again at 25 Hz for 3 min.

372 Homogenate was centrifuged for 15 min at 14,980g, 4 ºC. The centrifugation supernatant was

373 collected and dried in a Savant SPD111V (ThermoFisher Scientific) speedvac concentrator. The

374 centrifugation pellet was resuspended in 3:1 (by volume) dichloromethane/methanol solvent

375 mixture and further homogenized at 25 Hz for 5 minutes, followed by centrifugation at 14,980g

376 for 2 minutes. This latter centrifugation supernatant was collected and air dried. Both extracts

377 were stored at -80 ºC until LC-MS analysis.

378

379 **LC-MS/MS:** The dried samples were resuspended in 50% methanol (LC-MS grade) spiked with

380 2µM sulphadimethoxine as internal control, pooling aqueous and organic extracts together.

12

381 Liquid chromatography was performed using a ThermoScientific Vanquish UHPLC system

382 fitted with 1.7 µm 100 Å Kinetex C8 column (50 X 2.1 mm) (Phenomenex). Data-dependent

383 MS/MS (ddMS^2) experiments were performed on a Q Exactive Plus (ThermoScientific) high

384 resolution mass spectrometer, under the control of XCalibur and Tune software

385 (ThermoScientific). Ions were generated for MS/MS analysis in both positive and negative ion

386 mode using heated electrospray ionization (HESI) source. Calibration of the instrument was

387 performed using recommended commercial calmix from ThermoScientific. See supplemental

388 information (**Table S4-7**) for detailed instrumental parameters.

389

390 **LC-MS/MS data analysis:** Raw data was converted to mzXML format using MS Convert

391 software [29][30]. Processing of the resulting mzXML files was done in MZmine version 2.30 [31] (see

392 **Table S8** for parameters). Data was filtered to only retain MS1 scans that were present in at least

393 6 samples and were associated with MS2 spectra (and therefore could potentially be annotated).

394 Blank removal was performed, with a minimum three-fold difference between blank and samples

395 required in order for a feature to be retained. Total Ion Current (TIC) normalization was

396 performed in Jupyter notebook using R (http://jupyter.org). Principal coordinate analysis (PCoA)

397 was performed on the TIC-normalized MS1 data using the Bray-Curtis-Faith dissimilarity metric

398 in QIIME 1 [32], visualized using Emperor [33]. PERMANOVA calculations were performed on

399 Bray-Curtis-Faith distance matrices using the R package "vegan" [34]. The 3D GI tract model was

400 built to scale from pictures of GI tract samples collected from our mice, using SketchUp 2017

401 software. Data was plotted onto this 3D model using 'ili (https://ili.embl.de/) [35]. Feature

402 annotation was performed through molecular networking on the Global Natural Products Social

403 Networking (GNPS) platform [17] (see **Table S9** for detailed parameters). All annotations are

404 levels 2 or 3 according to the metabolomics standards initiative [36]. Molecular networks were

405 visualized using Cytoscape [37][38]. Venn diagrams were generated using:

406 http://bioinformatics.psb.ugent.be/webtools/Venn/. Random forest analysis [39] was performed in

407 Jupyter notebook using the randomForest R package and 7501 trees, classifying based on

408 infected vs uninfected status. All code can be accessed at https://github.com/mccall-lab-OU/GI-

409 tract-paper.

410

411   **16S method and data analysis:** DNA was extracted from homogenized tissue samples using the

412   DNeasy PowerSoil kit (Qiagen) following manufacturers protocols. The V4 hypervariable region

413   of the 16S rRNA gene was amplified using barcoded Illumina-compatible primers 515F and

414   806R as previously described [40]. The resulting amplicons were pooled in equimolar proportions

415   and sequenced on an Illumina MiSeq Instrument. Paired end sequencing reads were quality

416   filtered and merged to reconstruct the complete V4 region using AdapterRemovalV2 [41]. These

417   analysis-ready reads were used to identify operational taxonomic units (OTUs) following the

418   UNOISE pipeline implemented in Usearch v10 [42]. Taxonomy was assigned to the representative

419   OTUs using the EzTaxon database [43]. The resulting OTU table was rarefied to a depth of 5,000

420   reads per individual, and all downstream statistical analyses were performed using this rarefied

421   OTU table. Alpha- (observed species) and beta-diversity (unweighted UniFrac) analyses were

422   performed using scripts implemented in QIIME 1 [32]. Kruskal-Wallis tests with FDR correction

423   were used for comparison of genus-level taxonomic summaries to infection status and disease

424   stage.

425

426   **Additional statistical information:** All statistical tests are paired. Non-parametric tests were

427   used where possible (Mann-Whitney U-test), which makes no assumptions as to data normality.

428   No additional tests of normality were performed. For acylcarnitine data analysis and Figure 2

429   panels, where Mann-Whitney U-tests were performed for each sampling site, FDR correction

430   was performed to adjust for multiple comparison, as specified in the text and in figure legends.

431   Boxplots display first quartile, median and third quartile, with whiskers no more than 1.5 times

432   interquartile range.

433

434   **Data Availability:** Metabolomics data have been deposited on MassIVE, accession numbers

435   MSV000082614 (positive mode, oesophagus), MSV000082615 (negative mode, oesophagus),

436   MSV000082618 (positive mode, stomach), MSV000082619 (negative mode, stomach),

437   MSV000082612 (positive mode, small intestine), MSV000082613 (negative mode, small

438   intestine), MSV000082616 (positive mode, large intestine and cecum), and MSV000082617

439   (negative mode, large intestine and cecum). 16S data has been deposited in the NIH Short Read

440   Archive, project number PRJNA553060. Molecular networks can be accessed here:

441   https://gnps.ucsd.edu/ProteoSAFe/status.jsp?task=801f2cc53c504fad8e64a08565173309#

14

442   (positive mode networking from mzXML files; used for annotations and dataset matching);

443   https://gnps.ucsd.edu/ProteoSAFe/status.jsp?task=4592e7dfd96c440f8885fb312d50e124

444   (positive mode feature-based molecular networking; used to cluster MS1 data into chemical

445   families);

446   https://gnps.ucsd.edu/ProteoSAFe/status.jsp?task=d86b3d7c69c646479ef2cf5e7a432ba8

447   (negative mode networking from mzXML files; used for annotations and dataset matching);

448   https://gnps.ucsd.edu/ProteoSAFe/status.jsp?task=a6415577c1c24bc3823c9af5d9b5092c

449   (negative mode feature-based molecular networking; used to cluster MS1 data into chemical

450   families). Interactive 3D maps of metabolomic data for representative animals can be accessed

451   here: https://ili.embl.de/?ftp://massive.ucsd.edu/MSV000082614/updates/2019-07-

452   10_ehossain_cee84dec/other/3D model of mouse

453   2_ili.stl;ftp://massive.ucsd.edu/MSV000082614/updates/2019-07-

454   10_ehossain_cee84dec/other/Pos_m10_ili.csv (mouse 10, infected, acute-stage sample

455   collection) https://ili.embl.de/?ftp://massive.ucsd.edu/MSV000082614/updates/2019-07-

456   10_ehossain_cee84dec/other/3D model of mouse

457   2_ili.stl;ftp://massive.ucsd.edu/MSV000082614/updates/2019-07-

458   10_ehossain_cee84dec/other/pos_m18_ili.csv (mouse 18, uninfected, chronic-stage sample

459   collection). All code can be accessed at https://github.com/mccall-lab-OU/GI-tract-paper.

460

Acknowledgements:

470

Author contributions:

472   LIM designed the project. EH and LIM performed metabolite extractions and LC-MS

473   instrumental analysis. EH, CW, DL, MK, CG and LIM performed LC-MS data analysis. DL

474   built the 3D GI tract model. SLJ and DT performed *in vivo* experimentation, carnitine treatment,

475   and tissue sample collection. SK and CMW performed DNA extractions and 16S library builds.

476   KS performed the16S sequencing and analysis. LIM, EH and KS wrote the paper.

477

478   **References:**

479   1.   Bern, C. Chagas' Disease. *N. Engl. J. Med.* **373**, 456–466 (2015).

480   2.   Gascon, J., Bern, C. & Pinazo, M.-J. Chagas disease in Spain, the United States and other non-

481   endemic countries. *Acta Trop.* **115**, 22–27 (2010).

482   3.   Rassi, A., Jr, Rassi, A. & Marin-Neto, J. A. Chagas disease. *Lancet* **375**, 1388–1402 (2010).

483   4.   Tarleton, R. L. Trypanosoma cruzi and Chagas Disease: Cause and Effect. in *World Class Parasites*

484   107–115 (2003).

485   5.   Stanaway, J. D. & Roth, G. The burden of Chagas disease: estimates and challenges. *Glob. Heart* **10**,

486   139–144 (2015).

487   6.   Lewis, M. D. *et al.* Bioluminescence imaging of chronic Trypanosoma cruzi infections reveals

488   tissue-specific parasite dynamics and heart disease in the absence of locally persistent infection. *Cell.*

489   *Microbiol.* **16**, 1285–1300 (2014).

490   7.   Lewis, M. D., Francisco, A. F., Taylor, M. C., Jayawardhana, S. & Kelly, J. M. Host and parasite

491   genetics shape a link between Trypanosoma cruzi infection dynamics and chronic cardiomyopathy.

492   *Cell. Microbiol.* **18**, 1429–1443 (2016).

493   8.   Francisco, A. F. *et al.* Limited Ability of Posaconazole To Cure both Acute and Chronic

494   Trypanosoma cruzi Infections Revealed by Highly Sensitive In Vivo Imaging. *Antimicrob. Agents*

495   *Chemother.* **59**, 4653–4661 (2015).

496   9.   Stensvold, C. R. & van der Giezen, M. Associations between Gut Microbiota and Common Luminal

497   Intestinal Parasites. *Trends Parasitol.* **34**, 369–377 (2018).

498   10. McCall, L.-I. *et al.* Experimental Chagas disease-induced perturbations of the fecal microbiome and

499   metabolome. *PLoS Negl. Trop. Dis.* **12**, e0006344 (2018).

500   11. Patti, G. J., Yanes, O. & Siuzdak, G. Innovation: Metabolomics: the apogee of the omics trilogy.

501   *Nat. Rev. Mol. Cell Biol.* **13**, 263–269 (2012).

502   12. Mullard, A. 2018 FDA drug approvals. *Nature Reviews Drug Discovery* **18**, 85–89 (2019).

503   13. McCall, L.-I. *et al.* Mass Spectrometry-Based Chemical Cartography of a Cardiac Parasitic

504   Infection. *Anal. Chem.* **89**, 10414–10421 (2017).

505   14. Rassi, A., Jr, Rassi, A. & Marcondes de Rezende, J. American trypanosomiasis (Chagas disease).

506   *Infect. Dis. Clin. North Am.* **26**, 275–291 (2012).

507   15. Knubel, C. P. *et al.* Indoleamine 2,3-dioxigenase (IDO) is critical for host resistance against

508   Trypanosoma cruzi. *FASEB J.* **24**, 2689–2701 (2010).

509   16. Knubel, C. P. *et al.* 3-Hydroxy kynurenine treatment controls T. cruzi replication and the

510   inflammatory pathology preventing the clinical symptoms of chronic Chagas disease. *PLoS One* **6**,

511   e26550 (2011).

512   17. Wang, M. *et al.* Sharing and community curation of mass spectrometry data with Global Natural

513   Products Social Molecular Networking. *Nat. Biotechnol.* **34**, 828–837 (2016).

514   18. Wikoff, W. R. *et al.* Metabolomics analysis reveals large effects of gut microflora on mammalian

515   blood metabolites. *Proc. Natl. Acad. Sci. U. S. A.* **106**, 3698–3703 (2009).

516   19. Uchimura, Y. *et al.* Antibodies Set Boundaries Limiting Microbial Metabolite Penetration and the

517   Resultant Mammalian Host Response. *Immunity* **49**, 545–559.e5 (2018).

518   20. Robello, C. *et al.* The fecal, oral, and skin microbiota of children with Chagas disease treated with

519   benznidazole. *PLoS One* **14**, e0212593 (2019).

520   21. Planer, J. D. *et al.* Synergy testing of FDA-approved drugs identifies potent drug combinations

521   against Trypanosoma cruzi. *PLoS Negl. Trop. Dis.* **8**, e2977 (2014).

522   22. McCarville, J. L. & Ayres, J. S. Disease tolerance: concept and mechanisms. *Curr. Opin. Immunol.*

523   **50**, 88–93 (2018).

524 23. Lewis, M. D. & Kelly, J. M. Putting Infection Dynamics at the Heart of Chagas Disease. *Trends*

525 *Parasitol.* **32**, 899–911 (2016).

526 24. Tarleton, R. L. Chagas disease: a role for autoimmunity? *Trends in Parasitology* **19**, 447–451

527 (2003).

528 25. Rodrigues-Dos-Santos, Í. *et al.* Exploring the parasite load and molecular diversity of Trypanosoma

529 cruzi in patients with chronic Chagas disease from different regions of Brazil. *PLoS Negl. Trop. Dis.*

530 **12**, e0006939 (2018).

531 26. Vinolo, M. A. R., Rodrigues, H. G., Nachbar, R. T. & Curi, R. Regulation of Inflammation by Short

532 Chain Fatty Acids. *Nutrients* **3**, 858–876 (2011).

533 27. Sánchez-Valdéz, F. J., Padilla, A., Wang, W., Orr, D. & Tarleton, R. L. Spontaneous dormancy

534 protects Trypanosoma cruzi during extended drug exposure. *eLife* **7**, (2018).

535 28. Francisco, A. F. *et al.* Nitroheterocyclic drugs cure experimental Trypanosoma cruzi infections more

536 effectively in the chronic stage than in the acute stage. *Sci. Rep.* **6**, 35351 (2016).

537 29. Chambers, M. C. *et al.* A cross-platform toolkit for mass spectrometry and proteomics. *Nat.*

538 *Biotechnol.* **30**, 918–920 (2012).

539 30. Kessner, D., Chambers, M., Burke, R., Agus, D. & Mallick, P. ProteoWizard: open source software

540 for rapid proteomics tools development. *Bioinformatics* **24**, 2534–2536 (2008).

541 31. Pluskal, T., Castillo, S., Villar-Briones, A. & Oresic, M. MZmine 2: modular framework for

542 processing, visualizing, and analyzing mass spectrometry-based molecular profile data. *BMC*

543 *Bioinformatics* **11**, 395 (2010).

544 32. Caporaso, J. G. *et al.* QIIME allows analysis of high-throughput community sequencing data. *Nat.*

545 *Methods* **7**, 335–336 (2010).

546 33. Vázquez-Baeza, Y., Pirrung, M., Gonzalez, A. & Knight, R. EMPeror: a tool for visualizing high-

547 throughput microbial community data. *Gigascience* **2**, 16 (2013).

548 34. Dixon, P. VEGAN, a package of R functions for community ecology. *Journal of Vegetation Science*

549 **14**, 927 (2003).

18

550   35.   Protsyuk, I. *et al.* 3D molecular cartography using LC-MS facilitated by Optimus and 'ili software.

551   *Nat. Protoc.* **13**, 134–154 (2018).

552   36.   Sumner, L. W. *et al.* Proposed minimum reporting standards for chemical analysis. *Metabolomics* **3**,

553   211–221 (2007).

554   37.   Smoot, M. E., Ono, K., Ruscheinski, J., Wang, P.-L. & Ideker, T. Cytoscape 2.8: new features for

555   data integration and network visualization. *Bioinformatics* **27**, 431–432 (2011).

556   38.   Shannon, P. *et al.* Cytoscape: a software environment for integrated models of biomolecular

557   interaction networks. *Genome Res.* **13**, 2498–2504 (2003).

558   39.   Breiman, L. *Mach. Learn.* **45**, 5–32 (2001).

559   40.   Sankaranarayanan, K. *et al.* Gut Microbiome Diversity among Cheyenne and Arapaho Individuals

560   from Western Oklahoma. *Curr. Biol.* **25**, 3161–3169 (2015).

561   41.   Schubert, M., Lindgreen, S. & Orlando, L. AdapterRemoval v2: rapid adapter trimming,

562   identification, and read merging. *BMC Res. Notes* **9**, 88 (2016).

563   42.   Edgar, R. C. & Flyvbjerg, H. Error filtering, pair assembly and error correction for next-generation

564   sequencing reads. *Bioinformatics* **31**, 3476–3482 (2015).

565   43.   Yoon, S.-H. *et al.* Introducing EzBioCloud: a taxonomically united database of 16S rRNA gene

566   sequences and whole-genome assemblies. *Int. J. Syst. Evol. Microbiol.* **67**, 1613–1617 (2017).

567

568 **Figure legends:**
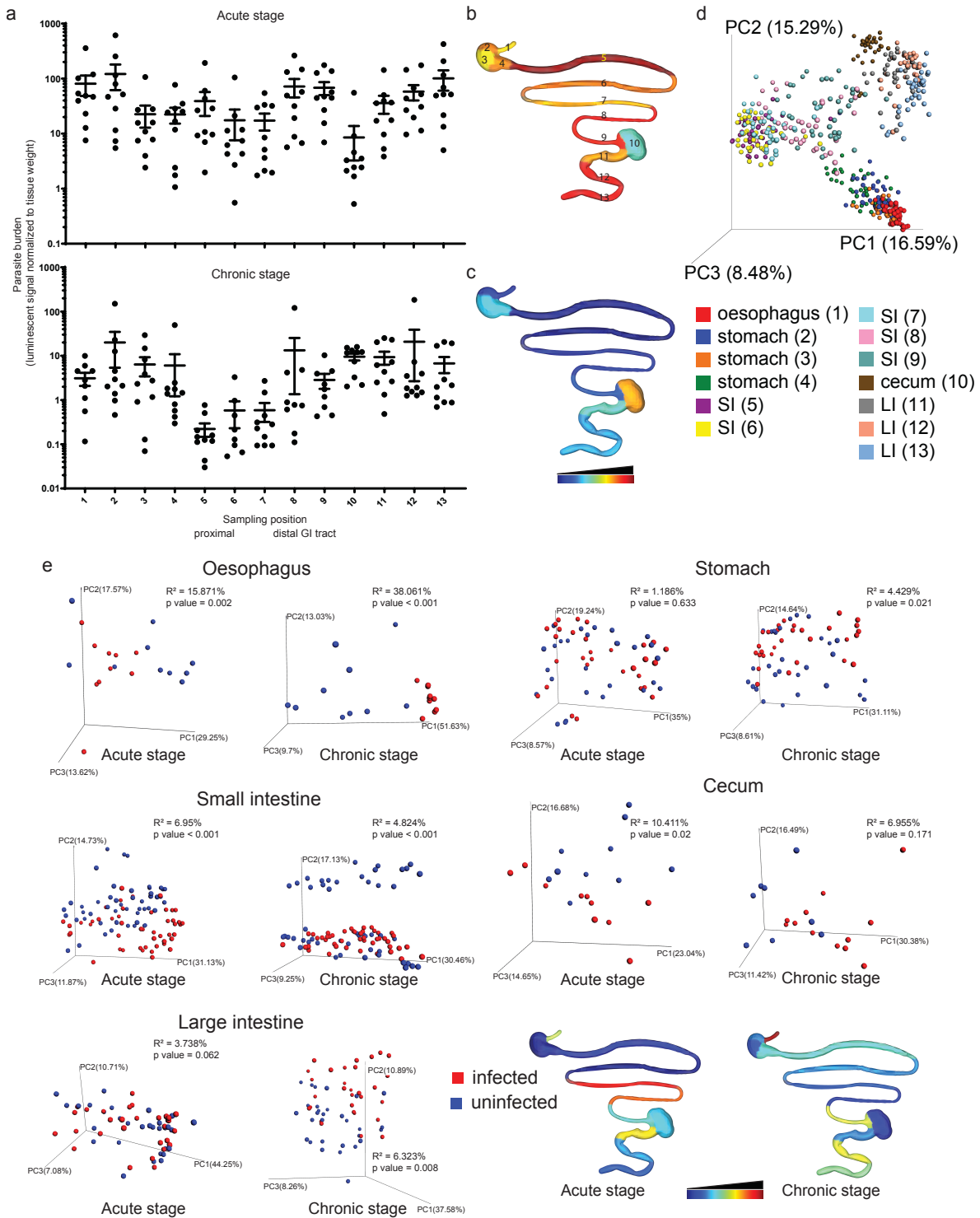
569 **Fig. 1. Spatial impact of *T. cruzi* infection is reflected by spatial modulation of the tissue**

570 **small molecule profile.** C3H/HeJ male mice (n=5 per group and per replicate) were mock-

20

571   infected or infected with 1,000 luminescent *T. cruzi* strain CL Brener trypomastigotes, in two

572   biological replicates. GI samples were collected 12 and 89 days post-infection. (a) Parasite

573   burden at each sampling site. GI was sectioned into 13 segments, and luminescence quantified at

574   each site. To correct for variations in sample size, luminescence counts were normalized to

575   sample weight, for each sample. Mean + standard error of mean are displayed. (b) Median

576   luminescent signal at each sampling site, 12 days post-infection. Sampling positions are

577   indicated. (c) Median luminescent signal at each sampling site, 89 days post-infection. Common

578   scale for b and c. (d) Principal coordinate analysis showing separation between sampling sites in

579   terms of overall chemical composition, even within a given organ (negative mode, all timepoints

580   combined, Bray-Curtis-Faith distance metric; $p<0.001$ R2=13.918%). (e) Principal coordinate

581   analysis showing significant chemical composition differences between infected and uninfected

582   samples in oesophagus (acute stage, PERMANOVA $p=0.002$, $R^2=15.871\%$; chronic stage

583   PERMANOVA $p<0.001$, $R^2=38.061\%$), stomach (chronic stage, PERMANOVA $p=0.021$,

584    $R^2=4.429\%$; non-significant acute stage), small intestine, (acute stage, PERMANOVA $p<0.001$,

585    $R^2=6.95\%$; chronic stage, PERMANOVA $p<0.001$, $R^2=4.824$), cecum (acute stage, PERMANOVA

586    $p=0.02$, $R^2=10.411\%$; non-significant chronic stage) and large intestine (chronic stage, PERMANOVA

587    $p=0.008$, $R^2=6.323\%$; non-significant acute stage). Bottom right-hand panels display R^2 at each

588   sampling site (common logarithmic scale, acute and chronic stage).

589

590

591
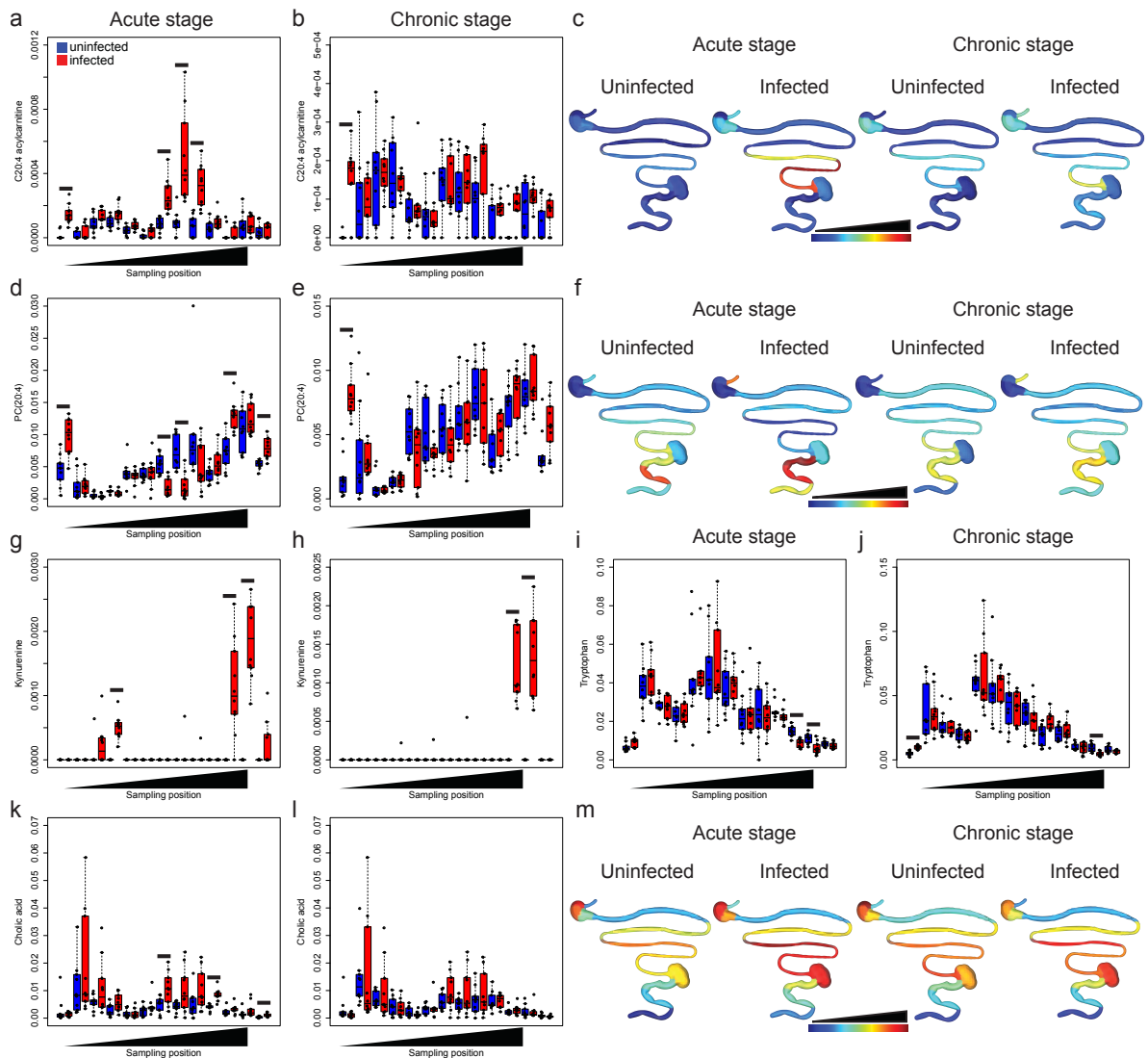
Fig. 2. Common and tissue-specific metabolic changes identified by random forest demonstrate persistence of these alterations at sites of CD. (a) and (b) Infection-induced elevation of C20:4 acylcarnitine in the oesophagus and small intestine in the acute stage, persisting in the oesophagus in the chronic stage (FDR-corrected Mann-Whitney p=0.000988, p=0.000141, p=0.00107, p=0.00107 for acute-stage positions 1, 7, 8 and 9; p=0.0188 for chronic-stage position 1). (c) Spatial distribution of C20:4 acylcarnitine (median, common linear scale). (d) and (e) Infection-induced elevation of PC(20:4) in the oesophagus and large intestine in the acute stage, persisting in the oesophagus in the chronic stage. PC(20:4) was decreased in the acute stage in the infected small intestine (FDR-corrected Mann-Whitney p=0.00189,

22

601   p=0.000844, p=0.00158, p=0.000844, p=0.000891 for acute-stage positions 1, 7, 8, 11 and 13;

602   p=0.000141 for chronic-stage position 1). (f) Spatial distribution of PC(20:4) (median, common

603   linear scale). (g) and (h) Infection-induced elevation of kynurenine in the stomach and large

604   intestine in the acute stage persists in the large intestine in the chronic stage (FDR-corrected

605   Mann-Whitney p=0.000796, p=0.00100, p=0.000796 for acute-stage positions 4, 11 and 12;

606   p=0.000415 and p=0.000415 for chronic-stage positions 11 and 12. (i) and (j) Infection-induced

607   decrease in tryptophan at sites of increased kynurenine in the large intestine (acute and chronic

608   stage). Infection also increased tryptophan in the oesophagus in the chronic stage. (FDR-

609   corrected Mann-Whitney p=0.001689 and p=0.0136 for acute-stage positions 11 and 12;

610   p=0.000281 and p=0.0253 for chronic-stage positions 1 and 12). All detected tryptophan adducts

611   combined. (k) and (l) Infection-induced increase in small intestine, cecum and large intestine

612   cholic acid (all detected adducts combined), acute stage only. (FDR-corrected Mann-Whitney

613   p=0.0498, p=0.000281, p=0.0297 for acute-stage positions 7, 10 and 13). (m) Spatial distribution

614   of cholic acid (median, common logarithmic scale). Black lines in panels (a-e) and (g-l) indicate

615   FDR-corrected Mann-Whitney p<0.05.

23

616
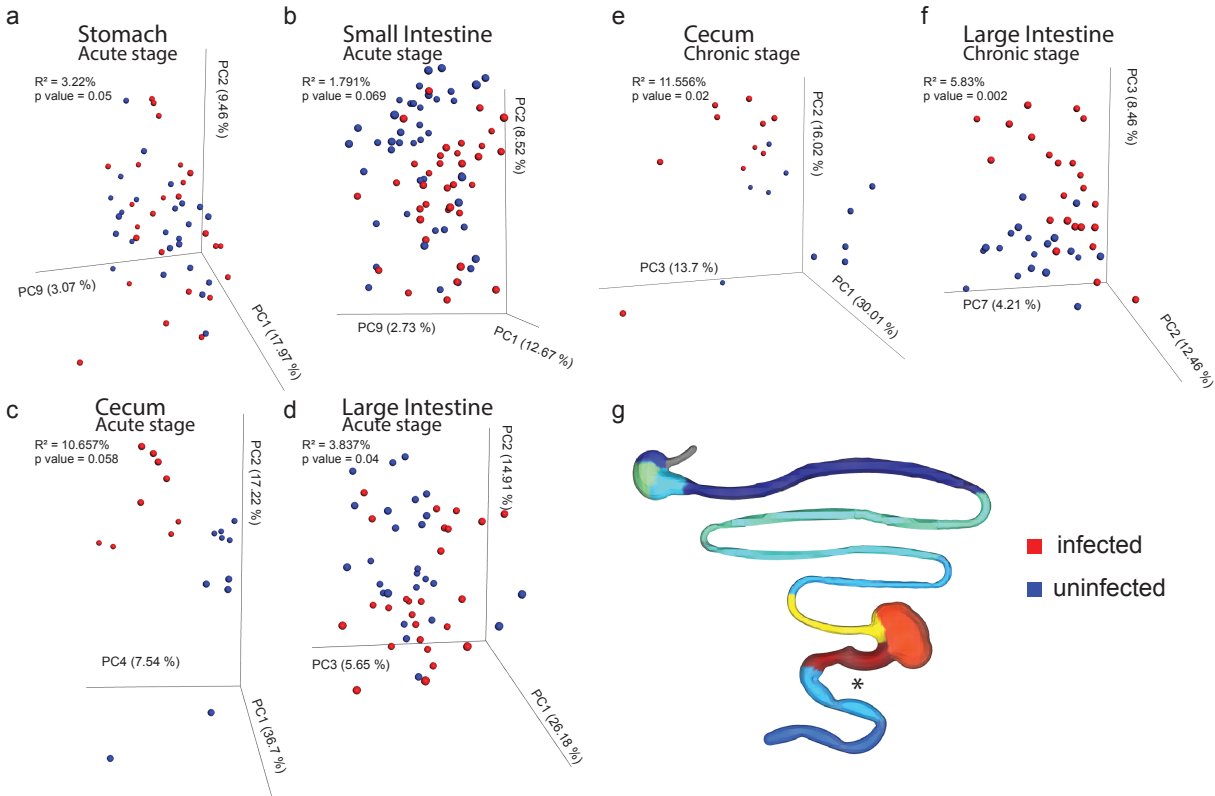
Fig. 3. Persistent, spatially heterogeneous impact of *T. cruzi* infection on the microbiota.
16S sequencing was performed on homogenate from all sampling sites except oesophagus in the acute stage, and focusing on large intestine and cecum in the chronic stage. Principal coordinate analysis revealed significant differences in the overall microbiota composition in the stomach (a) and large intestine (d) in the acute stage (PERMANOVA p=0.05, R^2=3.22% and PERMANOVA p=0.04, R^2=3.837%, respectively), which persisted in the chronic stage for the large intestine (f, PERMANOVA p=0.002, R^2=5.83%). Spatial heterogeneity was also observed within an organ (g), with the highest disturbances in the microbiota in the proximal large intestine (sampling position 11, PERMANOVA p=0.022, R^2=12.36% and PERMANOVA p=0.009, R^2=10.715% for acute and chronic stage, respectively). (g) displays R^2 at each sampling site in the acute stage (logarithmic scale). *, PERMANOVA p<0.05.

24

628
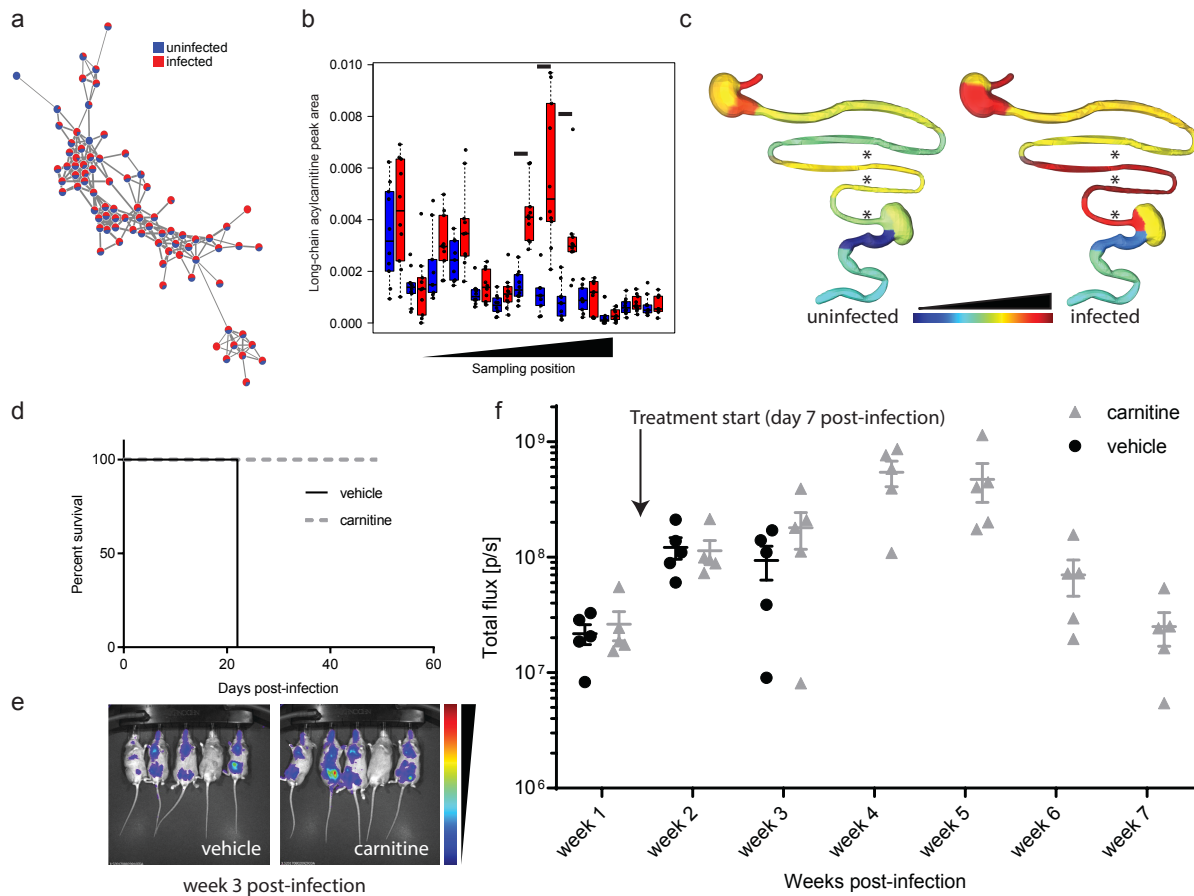
Fig. 4. Chemical cartography reveals a causal role for carnitine metabolism in acute CD tolerance. (a) Acylcarnitine molecular network, showing relative abundance of each detected acylcarnitine chemical family member (all tissue sites and timepoints combined; MS2 spectral count relative abundance). Each node represents one metabolite feature. Connected nodes are structurally similar (MS2 cosine score > 0.7), with edge thickness proportional to the cosine score. (b) Infection-induced increases in long-chain acylcarnitines in the distal small intestine 12 days post-infection (black lines indicate FDR-corrected Mann-Whitney p<0.05; p=0.000141, p=0.000563, p=0.000563 for positions 7, 8, 9, comparing infected and uninfected samples for the same positions) (c) Spatial distribution of median long-chain acylcarnitine peak area, 12 days post-infection (common logarithmic scale). Stars indicate sites of statistical significance, as displayed in panel b. (d) Carnitine treatment prevents acute-stage mortality. Male C3H/HeJ mice (n=5 per group) were infected with 50,000 luciferase-expressing *T. cruzi* strain CL Brener. Seven days post-infection, mice were switched to carnitine-supplemented drinking water (carnitine group; 1.3%; equivalent to 100 mg/kg/day based on water consumption) or continued on normal

25

643   drinking water (vehicle group). All vehicle-treated mice reached humane endpoints at 22 days

644   post-infection, whereas carnitine-treated mice survived the acute infection stage (p=0.0027,

645   Mantel-Cox test). (e) and (f) Comparable parasite burden was observed between carnitine-treated

646   and vehicle groups, indicating that carnitine's pro-survival effects represent disease tolerance

647   rather than antiparasitic efficacy. (e) Representative bioluminescent imaging, week 3 post-

648   infection (common scale). (f) Overall whole-body luminescence, weeks 1-7 post-infection. Mean

649   and standard error of mean are displayed.